# *Plasmonic Au-$MoO_3$ Colloidal Nanoparticles by Reduction of $HAuCl_4$ by Blue $MoO_x$ Nanosheets and Observation of the Gasochromic Property*

**M. A. Hosseini & M. Ranjbar**

**Plasmonics**

ISSN 1557-1955

Plasmonics
DOI 10.1007/s11468-018-0704-8


Springer

Plasmonics
https://doi.org/10.1007/s11468-018-0704-8

# Plasmonic Au-$MoO_3$ Colloidal Nanoparticles by Reduction of $HAuCl_4$ by Blue $MoO_x$ Nanosheets and Observation of the Gasochromic Property

M. A. Hosseini[1] · M. Ranjbar[1]

Received: 30 October 2017 / Accepted: 14 January 2018


**Abstract**
Defective colloids of blue $MoO_x$ nanosheets were prepared by anodizing exfoliation method in water. This colloidal solution exhibits an optical plasmonic absorption band in the infrared region at about 760 nm. Merely mixing $HAuCl_4$ solution with the $MoO_x$ leads to loss of the blue color, decaying of 760 nm plasmonic peak and simultaneous formation of the gold plasmon absorption peak at 550–570 nm. Some spectral variations in gold plasmonic peak and $MoO_x$ optical band gap were observed for Mo:Au ratio of 10:1, 20:1, 30:1, and 40:1. The size of the gold nanoparticles was in the 5–6 nm range with fcc crystalline structure. X-ray photoelectron spectroscopy (XPS) revealed that the initial solution contains $Mo^{5+}$ states and hydroxyl groups, which after reduction, hydroxyl groups are eliminated and the $Mo^{5+}$ states converted to $Mo^{6+}$. The obtained Au-$MoO_3$ colloids have a gasochromic property in which they are colored back to blue in the presence of hydrogen gas and the molybdenum oxide absorption peak recovered again. Furthermore, it was observed that both gold and Mo oxide plasmonic peaks redshift by insertion of hydrogen gas which is attributed to change in solution refractive index and formation of defect concentration.

**Keywords** $MoO_x$ nanosheets · Anodizing exfoliation · $HAuCl_4$ · Gold nanoparticles · Localized surface plasmon resonance · Gasochromic · TEM · XPS

## Introduction

GNPs have many applications in biological and chemical sensing due to surface plasmon resonance and negligible toxic properties [1–4]. Synthesis of gold nanoparticles with different shape and size has become one of the most interesting research topics now [5–8]. Gold nanoparticles are usually prepared by chemical reduction of gold precursors, commonly $HAuCl_4$, with a variety of reducing agents like citrate [9], amino acids [10], ascorbic acid [11], and sodium borohydride [5]. In addition to single GNPs, many works have been devoted to synthesis of gold-metal oxide compositional nanoparticles [12–14]. For the reduction of gold precursors to metallic nanoparticles, use of preformed different nanoparticles seeds as nucleation center are crucial [15–21].

Recently, scientists have paid much attention to the 2D metal oxide nanomaterials due to their unique physical and chemical properties [22–25]. Molybdenum oxide is one of the dichalcogenides, forming nanosheets of 2D structures due to weak Van der Waals bonds between lattice planes. The quantum size effects in 2D materials allow shifts in electronic structure and oxidation potentials so that permits enhanced catalytic activities not possible in bulk. Especially in 2D materials, edge-site substitution with metals and nucleation and growth of metal NPs is possible due to the high density of defect-containing reactive edges [26]. Therefore, they may be a good candidate for use as the primary nucleus for the reduction of $HAuCl_4$. On the other hands, it is believed that surface defect sites play a key role in catalytic activity of molybdenum oxide, either as nucleation centers or as attachment sites [27]. Therefore, in addition to two-dimensionality, the evolution of defects in molybdenum oxide nanosheets can enhance its catalytic activity towards a metal precursor and is often performed by reducing the fully oxidized $MoO_3$ [28–30].

Until now, several methods have been developed for 2D materials synthesis. In the case of 2D $MoO_3$, exfoliation of bulk $MoO_3$ is a common method which includes liquid [31] and micro-mechanical exfoliation [32]. The liquid-phase exfoliation method deals with the intercalation of ions of the solution into the gaps of weakly bonded inter-layers of

✉ M. Ranjbar
ranjbar@cc.iut.ac.ir

[1] Department of Physics, Isfahan University of Technology, Isfahan 84156-83111, Iran

Published online: 01 February 2018

$MoO_3$. Breaking of inter-layer bonds causes exfoliation of plate-like structures and dispersion of the exfoliated pieces into a suspension. Needing a long time and embedding impurity are the main problems of liquid-phase exfoliation of bulk $MoO_3$. Oxidation of metals without annealing in an oxidizing atmosphere is a remarkable idea for 2D growth that fewer attentions have been paid to. Previously, we have demonstrated that a blue colloidal solution of $MoO_{x(x<3)}$ nanosheets, where the blue color is an evidence for extensive structural defects, can be synthesized via an anodizing-exfoliation process as a facile, mass productive, and rapid method [33, 34]. Thanks to Mo incomplete oxidation, oxygen defects have been created, which are responsible for the blue color as well as the Mo oxide ability towards reduction the $Pd^{2+}$ cations into metallic Pd which was accompanied by losing the blue color at room temperature. XPS has indicated that this is an oxidation reduction reaction that governs this chemical conversion. The obtained Pd-$MoO_3$ colloidal solutions have shown unique gasochromic and photochromic properties in liquid phase. In principle, Mo has three different oxidation states: $Mo^{6+}$, $Mo^{5+}$, and $Mo^{4+}$ that two later states concern oxygen vacancies and promote the reduction reaction by electron donating to supported cations. On the other hands, both Au and Mo oxide, as a single particle or multi-particle systems, have become more interesting todays for their applications in catalysts [27], solar [35], localized surface plasmon resonance (LSPR) [36, 37], and sensing [38]. As one of a new aspect, both gold and molybdenum oxide exhibit LSPR effect in which the absorption of gold lies often within visible range and that of Mo oxide within NIR region. In addition to plasmonic behavior, Mo oxide exhibits gasochromic switching as an interesting effect in some transition metal oxides in which the color of the material changes to an absorbing state in a catalytic interaction with hydrogen gas due to developing oxygen defects [39–42]. In the gasochromic coloration of W and Mo oxides, the coloration is accompanied by arising one or several plasmonic absorption peaks. So, combination of plasmonic property of gold and plasmonic-gasochromic effect of Mo oxide allows a wide range of spectral variations from visible to NIR region in the presence of hydrogen, which can be also used for optical hydrogen gas sensing.

While, there is a significant number of articles on the bulk or thin films of this composition fabricated via different synthesis and deposition methods [43–47], a few reports exist on colloidal Au-$MoO_3$ systems to our best knowledge. Thus, the main contribution of this work is to examine the ability of blue $MoO_x$ nanosheets reduction for a gold salt precursor to produce Au-$MoO_3$. In this work, we demonstrate that Au-$MoO_3$ colloids are achievable by reduction of gold salt solution with exfoliated blue $MoO_x$ nanosheets. Furthermore, anodizing exfoliation is a simple and rapid method for synthesis a variety of metal oxides colloids and needs to be more investigated. Herein, we observed formation of gold nanoparticles of several nanometers in size in addition to oxidation of blue molybdenum oxide and its losing plasmonic peak. The produced Au-$MoO_3$ colloidal nanoparticles are also able to exhibit gasochromic coloration property with a spectral shifting aspect in the presence of hydrogen gas.

## Experimental

The fabrication method of Mo oxide was similar to that used in our previous report [33]. Colloidal nanoparticles of molybdenum oxide were prepared via an electrochemical anodizing of Mo sheets in a 0.02 M HCl electrolyte (Fig. 1). In this process, two molybdenum sheets were put 1 cm apart from each other. A 30 V DC bias voltage was applied to the two ends of sheets for 5 min. By applying voltage, the anode began to corrode electrochemically, gradually dispersed into the electrolyte and a colloidal solution was obtained. Total dispersion of molybdenum was measured from the weight loss of molybdenum sheets. $HAuCl_4$ ($10^{-4}$ mM) aqueous solution was prepared by dissolving 0.039 g hydrogen tetrachloroaurate (III) hydrate (99.9%, metals basis, Au 49% min., Alfa Aesar) in 1000 ml DI water and 0.1 ml HCl. By merely mixing of hydrogen tetrachloroaurate (III) hydrate solution with the colloidal molybdenum oxide, samples of different $MoO_x$:$HAuCl_4$ ratios (Mo:Au = 10:1, 20:1, 30:1, and 40:1) were obtained and named according to Mo:Au ratio (for example Mo:Au = 10:1 denoted $MA_{10:1}$). The schematic representation from anodizing exfoliation of Mo sheets to $HAuCl_4$ reduction by blue $MoO_x$ nanosheets is presented in Fig. 1. Optical absorptions were measured in the 200–1100 nm wavelength range using Perkin Elmer spectrophotometer (Lambda 25). We characterized samples by XRD using a Philips XPERT X-ray diffractometer unit with $Cu_{K\alpha}$ radiation at a scanning speed of 5° per minutes. The morphology and particle size were determined by TEM imaging using Philips Holland model CM120. The XPS analyses were done using an ESCA/AES system (CHA, Specs model EA10 plus). The binding energy of carbon (284.8 eV) was used for calibration energy scales. The electrochemical experiments were performed with a potentiostat unit of Iviumstat which were conducted in a three-electrode electrochemical cell with Pt wire and Ag/AgCl (satd KCl) electrodes as the counter and reference electrodes in a 1 M $H_2SO_4$ electrolyte solution at ambient temperature. The samples were drop-casted over a graphite plate (1 × 1 $cm^2$). The cyclic voltammetry (CV) measurements of the samples were performed in the potential range of 0 to 0.6 V at a scan rate of 10 $mVs^{-1}$. FTIR was performed in the 400–4000 $cm^{-1}$ range using a Perkin-Elmer 2000 system instrument. In order to perform XRD, FTIR, XPS, CV characterizations, samples were prepared by centrifuging followed by drop-casting over quartz or graphite substrates. Gasochromic coloration experiments were conducted by

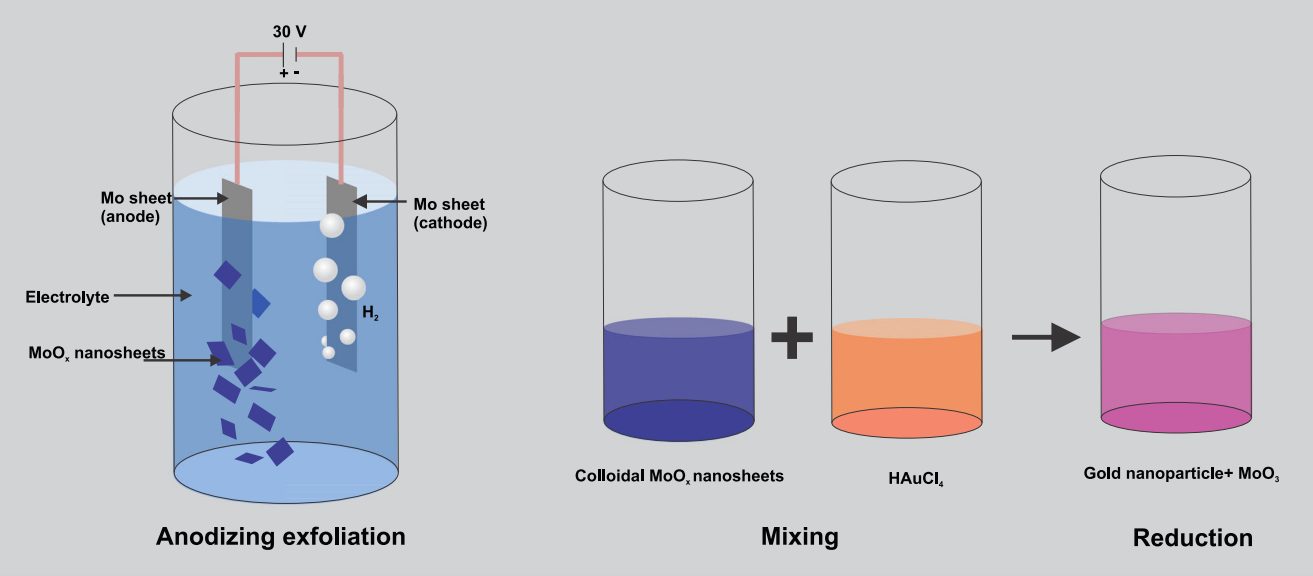


**Fig. 1** Schematic representation of anodizing exfoliation of Mo sheets and obtaining blue $MoO_x$ nanosheets, mixing with HAuCl4 process and formation of Au+$MoO_3$ nanoparticles and reduction processes of $HAuCl_4$ by the blue $MoO_x$

injection of 10%H2/Ar mixed gas. To do this, a tiny glass pipe was inserted into a sealed quartz cell containing the solution.

## Result and Discussion

Figure 2a illustrates the optical absorption spectra of the $HAuCl_4$ solution, as-prepared blue $MoO_x$ colloids before and after mixing with the $HAuCl_4$ in four different Mo:Au ratios of 10:1, 20:1, 30:1, and 40:1. For the spectrum of blue $MoO_x$ in Fig. 1, the plasmonic behavior concerns a broad optical absorption band observable in the NIR region at ~ 760 nm, which originates from the presence of oxygen vacancies [48] and as a metal oxide semiconductor, it represents an absorption edge under 400 nm due to excitation across the optical band gap. Furthermore, the $HAuCl_4$ has a characteristic peak around 300 nm.

As can be seen, the mixing of these two solutions results in formation of gold plasmon absorption peak at about 550 nm, indicating the gold precursor reduces to GNPs which can also be viewed from the appearing a pink color in the photographic image. In addition, the $HAuCl_4$ peak decays for all the mixing ratios after the mixing process, thus indicating the gold precursor decomposes completely.

Formation of GNPs is understandable according to diffraction gold diffraction peaks in the XRD patterns. The XRD patterns of the initial blue $MoO_x$, samples $MA_{10:1}$ and $MA_{40:1}$ are shown in Fig. 4(a–c), respectively. No diffraction peak exists over the pattern of $MoO_x$ in part (a), which will be explained by two-dimensionality of the $MoO_x$ nanoflakes

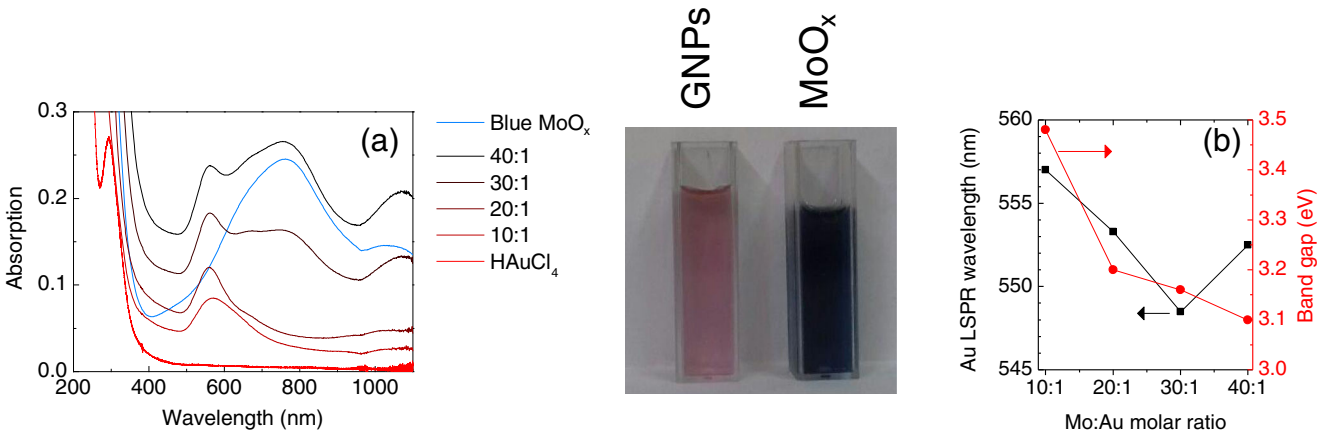


**Fig. 2** **a** Optical absorption spectra of initial blue $MoO_x$ nanosheets colloidal solution, $HAuCl_4$ solution and after their merely mixing at different Mo:Au ratio of 10:1, 20:1, 30:1, and 40:1. Photographic images of the solutions are also presented in the middle panel. Blue $MoO_x$ spectrum shows a broad LSPR peak at 760 nm. After a mixing step, GNPs are synthesized via a $HAuCl_4$ reduction with about 550 nm LSPR peak position. **b** Au LSPR peak position and MoOx optical band gaps as a function of Mo:Au mixing ratio

(TEM images in the next part). However, apparent diffraction peaks of fcc Au (JCPDS No. 00-001-1172) appears for samples $MA_{10:1}$ and $MA_{40:1}$. The sharpest peak at (111) direction suggests that Au nanoparticles are likely more developed along this direction [49].

The gold absorption wavelength (~550 nm) in Fig. 2 suggests that the particle size should be smaller than 20 nm [31] in agreement with the TEM results in the next section. Moreover, gold plasmon peak position, plotted vs. Mo:Au molar ratio in the left vertical axis of Fig. 2b, demonstrates blue-shift by increasing the Mo:Au ratio followed by a redshift at ratio 40:1. This spectral shift is mainly attributed to a reaction-induced variation in the solution refractive index, where the gold peak position can be used as an indicator for environment refractive index according to the following equation [31]:

$$\lambda_{max} = \lambda_p \sqrt{1 + 2n_m^2} \quad (1)$$

in which $\lambda_{max}$ is the gold peak position, $\lambda_p$ is bulk plasmon resonance wavelength and $n_m$ is refractive index of the medium. Right vertical axis of Fig. 2b indicates the measured $MoO_x$ optical band gap using Tauc method. Typically, the optical band gap depends on several factors, mainly oxidation degree of the metal oxide, so that it is expected to be minimized by increasing oxygen vacancies. The optical band gap, $E_g$, of the initial blue molybdenum oxide was measured to be ~2.8 eV. As can be seen, $E_g$ has been increased to about 3.5 eV for sample $MA_{10:1}$ which according to the values reported in the literature [50] indicating fully oxidation of the blue molybdenum oxide. By increasing the molybdenum ratio in samples 20:1 to 40:1, one can see a decrease in band gap, which is attributed to the presence of some unoxidized $MoO_x$ in high Mo:Au ratio.

TEM images and corresponding size distribution histograms are shown in Fig. 3a–c for the initial blue $MoO_x$, samples $MA_{10:1}$ and $MA_{40:1}$, respectively. The two dimensional nature of $MoO_x$ colloids is identified from the TEM image in part (a) where most of observable flakes look transparent, thus indicating that their thickness is only few nanometers. This is probably why there are no peaks in the XRD patterns (Fig. 4). From the size distribution histogram, an average lateral size of 24 nm was measured for the nanoflakes. In TEM images of samples $MA_{10:1}$ ad $MA_{40:1}$ (part (b) and (c)) two different kinds of particles exist. Those few particles that are bigger and seem darker are attributed to $MoO_3$ while those of smaller dimension are attributed to GNPs. One can see that these GNPs are uniformly distributed and the corresponding size distribution histograms indicate that the gold averages sizes are ~6.5 and 4.5 nm in sample $MA_{40:1}$ and $MA_{10:1}$, respectively, consistent with LSPR wavelength position in the absorption spectra. Partial formation of core-shell structure is also expectable because insets of Fig. 3 reveal a core-shell structure with about a 4-nm shell.

The chemistry of outermost layers of $MoO_x$ is more meaningful for catalytic reactions that may take place in the reduction of $HAuCl_4$. Therefore, to investigate the surface chemical states of elements in Au-$MoO_x$ colloids, XPS measurements were conducted. Figure 5 illustrates the high-resolution XPS spectra for the initial blue $MoO_x$ colloids and samples $MA_{40:1}$. Binding energies and FWHM of XPS peaks are presented in Table 1. As shown in Fig. 5a, the $Mo_{3d}$ transition for $MoO_x$ sample is fitted into two doublets, for which the Mo3d doublet at 235.7 and 232.6 eV binding energies corresponds to $Mo^{6+}$ and that at 234.7 and 231.6 eV to $Mo^{5+}$ [51, 52]. Comparison of binding energies and FWHMs in Table 1 reveals that the Mo3d peaks become narrower after reduction due to losing $Mo^{5+}$ peak contribution, which confirms conversion of 5+ states to 6+ as a result of oxidation. Au4f region has one doublet with peaks at 83.4 eV ($Au4f_{7/2}$) and 87 eV ($Au4f_{5/2}$) characteristic of metallic gold [53] in agreement with the results of XRD. Figure 5a–c right panels show the O1s XPS spectra of our samples. Generally, $O_{1s}$ region can deconvoluted into two peaks, one at binding energy about 530 eV related to oxygen in covalence bonds (metal-O in metal oxide) and another at about 532 eV related to hydroxyl groups (metal-OH) [53, 54]. For $MoO_x$ colloids, one can see that the hydroxyl peak is much stronger in comparison to O-metal bond, indicating the presence of a large quantity of hydroxyl group. However, the hydroxyl peak intensity considerably reduces after the mixing with $HAuCl_4$ in sample $MA_{40:1}$ indicating significant OH desorption during the reduction process. The role of hydroxyl groups in $HAuCl_4$ reduction to metallic GNPs have been reported elsewhere. For example, the commercially available PVP has been served as a reducing agent thanks to its hydroxyl end groups [55]. Therefore, it is expected that in addition to the role of oxygen defect, the hydroxyl groups existing in the structure of two dimensional $MoO_x$ nanoflakes play also role in its ability to reduce a noble metal salt. Using the peak area of $O_{1s}$ related to O-metal and all those of the $Mo_{3d}$, the O/Mo ratio is estimated to be 2.3 and 2.5 in the $MoO_x$ and $MA_{40:1}$, respectively, which confirms the defective nature of the initial blue sample or when concentration of $MoO_x$ is high (sample $MA_{40:1}$).

Electrochemical investigations were carried out for a better investigation of the oxidation of Mo oxide in our reduction process. Figure 5c right panel shows a typical CV curve of drop-casted solution of blue $MoO_x$ and sample $MA_{40:1}$ over the graphite plates as the working electrode in 1 M $H_2SO_4$ electrolyte. There are three distinct redox peaks in the curve of blue $MoO_x$ oxide located at 77/122, 162/202 and 380 mV/346 mV in the CV curve that are attributed to $Mo^{5+}/Mo^{6+}$, $Mo^{4+}/Mo^{6+}$, and $Mo^{4+}/Mo^{6+}$ transitions, respectively. The intensity of $Mo^{5+}/Mo^{6+}$ redox peak is relatively high for the blue $MoO_x$ sample before reduction in the mixing stage while it is almost eliminated after the reduction reaction. The higher electrical current for this peak is due to the presence of much

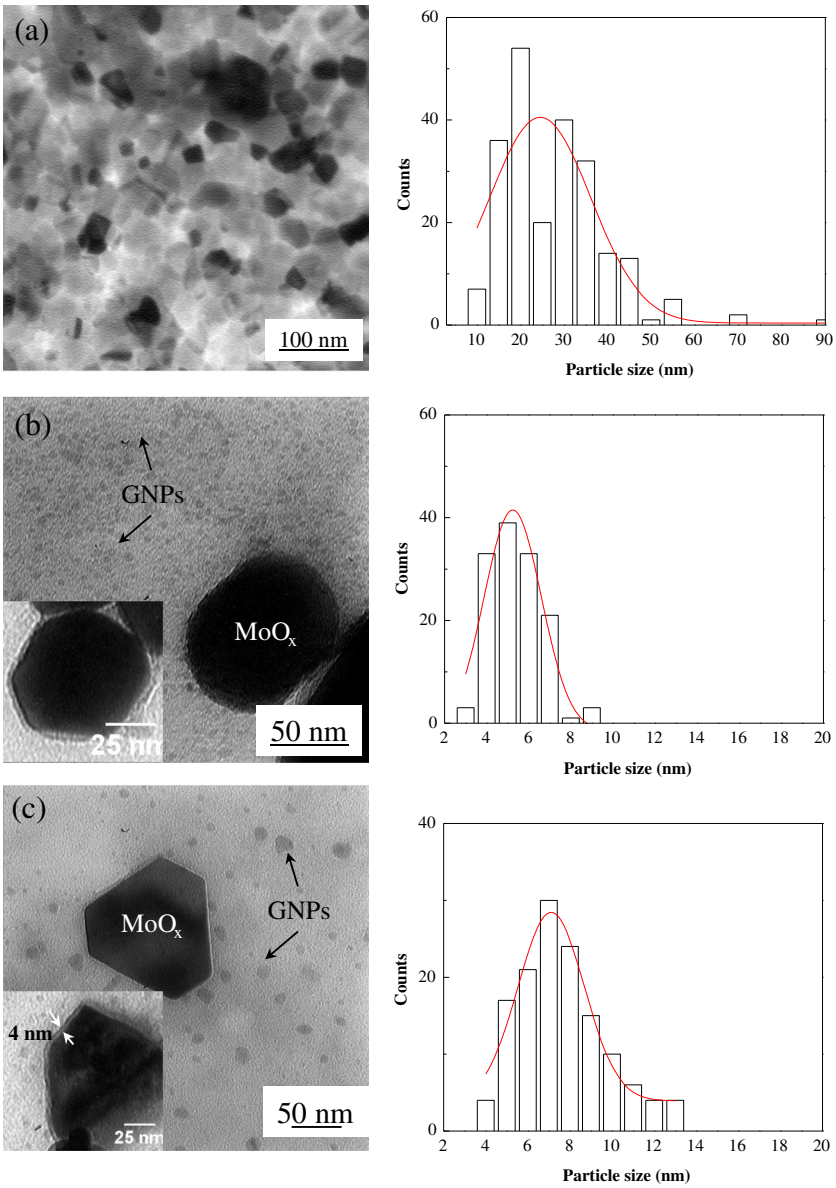


**Fig. 3** TEM images and size distribution histograms of **a** initial $MoO_x$ nanosheets, **b** sample $MA_{10:1}$, and **c** sample $MA_{40:1}$. Insides of part **b** and **c** show formation of $MoO_x$@Au core-shell structures with about 4 nm shell thickness

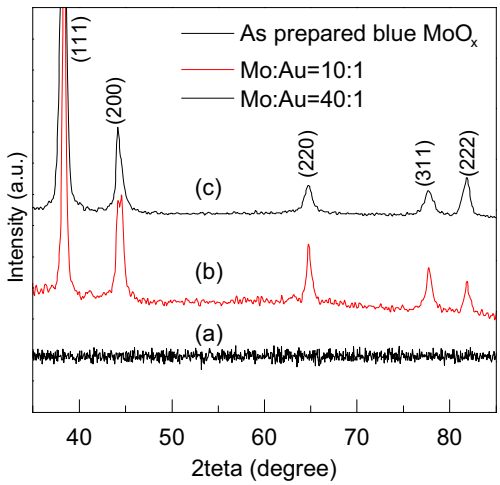


**Fig. 4** XRD patterns of (a) initial $MoO_x$ nanosheets, (b) sample $MA_{10:1}$, and (c) sample $MA_{40:1}$. FCC gold was detected by XRD patterns

concentration of $Mo^{5+}$ cations in the blue $MoO_x$ colloidal solution and the lower current for after mixing is in agreement with the XPS result concerning the lowering of $Mo^{5+}$ concentration [56, 57]. Therefore, XPS and CV confirm oxidation of blue molybdenum oxide.

FTIR spectroscopy was applied to investigate the variation in bonding related to $MoO_x$ nanosheets before and after reduction. FTIR spectra of initial blue $MoO_x$, sample $MA_{40:1}$ and $MA_{10:1}$ in the 400–4000 $cm^{-1}$ are presented in Fig. 6. Vibration around 562 $cm^{-1}$ is assigned to the stretching mode of the triply coordinated oxygen resulted from the edge-shared oxygen in common with three $MoO_6$ octahedral [51], which becomes broader after reduction. The peaks at 750 $cm^{-1}$ assigned to Mo–O–Mo vibrations of $Mo^{5+}$ states, which almost vanishes in sample $MA_{10:1}$ confirming conversion of 5+ oxidation states to 6+ states. The peaks in the range of 875–

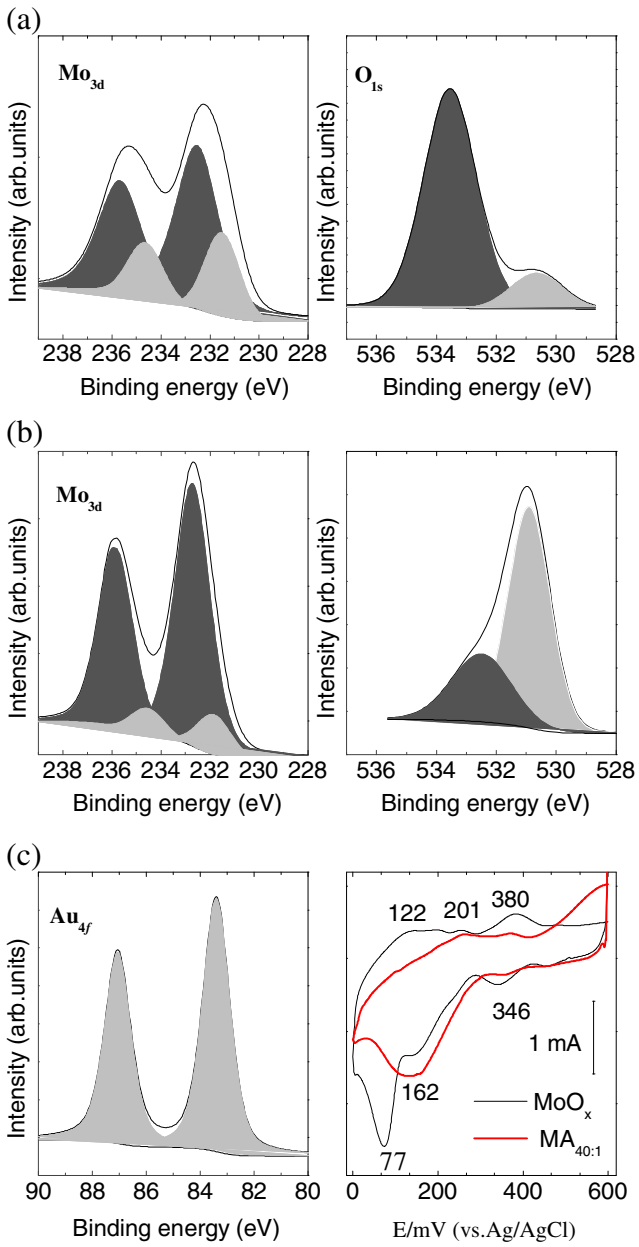


**Fig. 5** High resolution XPS spectra of $Mo_{3d}$, $O_{1s}$, and $Au_{4f}$ regions. **a** Initial $MoO_x$ nanosheets. **b** Sample $MA_{40:1}$. **c** Left panel: typical Au4f XPS spectrum and right panel: comparison of cyclic voltammetry of initial blue $MoO_x$ nanosheets and after reduction process. Absence of anodic peak at 77 meV after reducing $HAuCl_4$ confirms oxidation of molybdenum

1000 $cm^{-1}$ were attributed to the doubly cation-bonded oxygen atoms (Mo = O) [51]. Low relative spectral intensities of these peaks in sample 40:1, and almost it is vanishing in sample $MA_{10:1}$ show the effective role of gold salt on oxidation of the blue molybdenum oxide. In addition, some vibrations peaks were detected in the range of 1000–1450 $cm^{-1}$. They were associated with the vibration mode of the δMo–OH bending vibrations [58]. The broad bands at about 3425 and 1616 $cm^{-1}$ are O-H stretch and the bending of physisorbed water [58].

**Table 1** : XPS binding energies and corresponding FWHM of different elements

| Sample | B.E (eV)<br>FWHM (eV) | | |
|---|---|---|---|
| | $Mo3d_{3/2}$-$Mo3d_{5/2}$ | $O_{1s}$ | O/Mo |
| Blue $MoO_x$ | 235.7–232.6<br>234.7–231.6<br>2.5–2.5 | 533.5–530.7<br>2.1–2.0 | 2.3 |
| $MA_{40:1}$ | 235.7–232. 7<br>234.6–231.9<br>2.0–1.8 | 532.3–530.9<br>1.9–1.6 | 2.5 |

## Gasochromic Coloration

The Au-$MoO_x$ colloids, made by the reduction method of this paper, exhibited a considerable gasochromic response in which a color change from transparent to blue occurs upon bubbling %10 hydrogen gas. In Fig. 7a–d, spectral time variations for Mo:Au ratios of 10:1, 20:1, 30:1, and 40:1, are displayed at time intervals of 15 min. Before gas injection, the gold LSPR peak dominates the spectrum, while there is no significant absorption in the NIR region. Upon exposure to 10%$H_2$/Ar at room temperature, a drastic rise in the absorption peak occurs in the NIR region for all the samples, which demonstrate formation of the $MoO_x$ LSPR peak. Usually, the gasochromic developing process takes few minutes and a change from colorless to blue color can be observed during gas exposure, even after cutting off the gas exposure. Photographic images in Fig. 7 show that the pink color of Au-$MoO_3$ sample turns blue after hydrogen injection in a sealed quartz cell. This gasochromic behavior has been related to the reduction of Mo by hydrogen atoms spilt-over [59] and

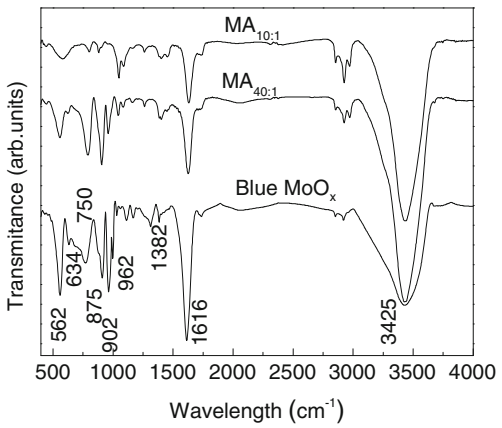


**Fig. 6** FTIR spectra of initial $MoO_x$ nanosheets, sample of $MA_{10:1}$, and sample of $MA_{40:1}$

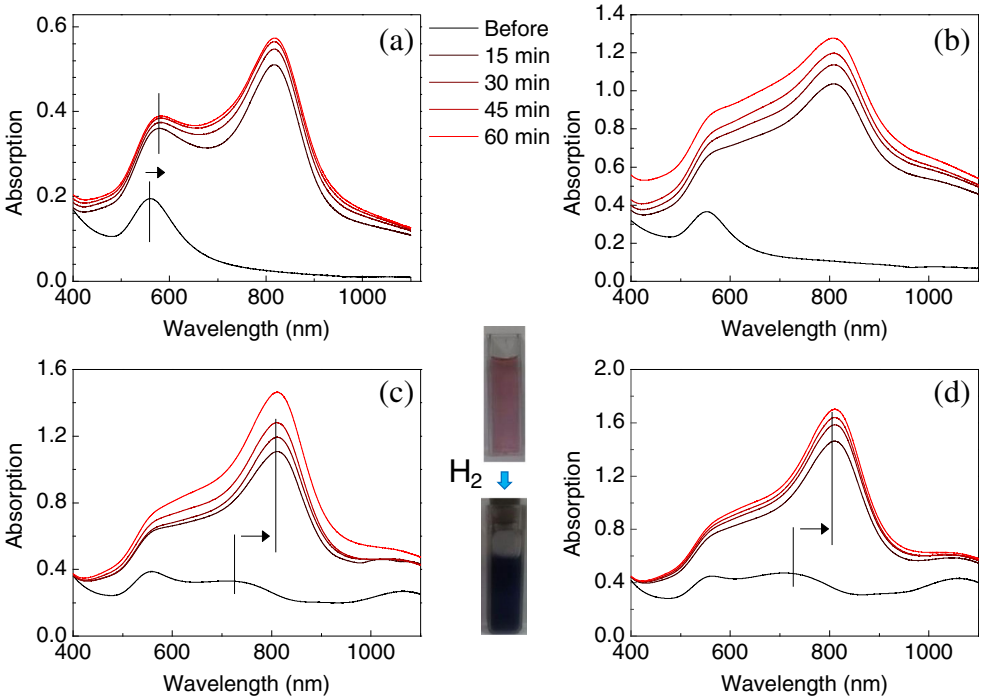


**Fig. 7** **a**–**d** Spectral time variations of Au-Mo oxide samples in the gasochromic process for Mo:Au ratios of **a** 10:1, **b** 20:1, **c** 30:1, and **d** 40:1, at hydrogen (10%) injection time intervals of 15 min. The LSPR spectral shift occurs for both gold and Mo oxide plasmonic peaks as shown by arrows. Typical photographic images for before and after hydrogen injection are shown for sample $MA_{30:1}$

as a result, oxygen defect develops into the Mo oxide lattice and the fully oxidized particles recover the $MoO_{x<3}$ composition. Partial reduction of $Mo^{6+}$ cations to $Mo^{5+}$ is also expected according to $MoO_3 + (3\text{-}x)H_2 \rightarrow MoO_x + (3\text{-}x)H_2O$ reaction. The gold nanoparticles in these systems can promote the room temperature dissociation of $H_2$ into H atoms and accelerate the coloration of Mo oxide colloids. The gold LSPR curve is integrated as a shoulder into the spectrum. It can be clearly seen that with the coloring time, the LSPR peak of molybdenum oxide dominates the spectrum and its intensity increases with Mo:Au ratio.

As the intensity of Mo oxide plasmonic peak increases upon gas exposure, the LSPR curve of gold shifts towards red wavelengths, which implies that the resonance wavelength increases. This noticeable redshift, shown in the Fig. 7a, for gold, plasmonic peak is about 20 nm for sample $MA_{10:1}$. As before, this redshift is due to the change in the dielectric constant in the solution on exposure to gas because the electrical, chemical, and optical properties of Mo oxide change in the presence of hydrogen. This is probably accompanied by an increase in the refractive index of the solution environment (gold surrounding) due to the coloration of molybdenum oxide.

Another LSPR redshift is observed for Mo oxide plasmonic peak after interacting with hydrogen gas, which is remarkably high (about 50 nm). This shifting is shown in samples $MA_{30:1}$ and $MA_{40:1}$ with arrows. In the case of plasmonic metal oxides, not only the shape, size, and environment of the nanoparticles affect the location of the peak, but also the level of oxygen defects is also effective in such a way that the wavelength reduces by defect concentration [60–62]. Therefore, the observed redshift can be partially due to the difference in the concentration of defects in the initial defective blue colloids obtained in exfoliation process and those created in the hydrogen gasochromic coloration process.

These aspects (Mo oxide peak-rise and plasmonic peak-shifts in both Au and $MoO_x$ absorption) can provide a high sensitivity of this solution for optical hydrogen sensing that can result from a combination of both change in plasmonic properties of the individual core-shell particles and the modification of colloidal environment due to change of dielectric constants of single nanoparticles' surrounding. The structural variations from the chemical reaction between hydrogen and Mo oxide can result oxygen defects and a shift in the fermi level position, resulting in a change in refractive index of Mo oxide. These changes affect the LSPR properties of both the plasmonic materials, producing spectral shifts of plasmonic resonance. Therefore, gasochromic investigations indicate that the samples produced via the reduction of $HAuCl_4$ by the defective $MoO_x$ nanosheets have a hydrogen detection ability and the refractive index varies in with hydrogen injection.

The formation of Au-$MoO_3$ via reduction mechanism is considered as the follows. The blue $MoO_x$ nanosheets obtained by anodizing exfoliation have a lot of surface defect sites. Localized electrons in oxygen vacancy sites transfer to the positively charged gold ions, oxidizing $MoO_x$ and reducing gold ions to gold metal and gold nuclei formation, which are responsible for the formation of gold plasmonic peak and decay of $MoO_x$ peak. So, two-dimensionality and defects in our $MoO_x$ play a key role in its reducing ability. On the other

hands, coloration in the gasochromic process is attributed to defect reformation via hydrogen injection and oxygen removing from the $MoO_3$. When the initial $MoO_x$ blue color disappears, it is an oxidizing effect because it is known that fully oxidized $MoO_3$ colloids are colorless and the blue color of defect-containing Mo oxide compounds is correlated to the oxygen defects. According to the literature, $Mo^{5+}$ is commonly accepted to be responsible for the blue color and absorption in $MoO_x$ [56–58, 63, 64]. Therefore, losing the blue color (Fig. 2) is attributed to oxidation of $MoO_x$ which is accompanied by formation of gold metal:

$$\begin{aligned} Mo^{5+}(\text{blue color}) &\rightarrow Mo^{6+}(\text{Colorless}) + e^- \\ Au^{3+} + 3e^- &\rightarrow Au^0 \end{aligned} \quad (2)$$

The appearance of plasmonic peak around 800 nm upon $H_2$ exposure, related to the reduction of Mo oxide by hydrogen atoms via spill-over mechanism on the produced gold nanoparticles. As a result, oxygen defect develops into the Mo oxide lattice and the fully oxidized particles recover the $MoO_{x<3}$ composition. Partial reduction of $Mo^{6+}$ cations to $Mo^{5+}$ is also expected according to the following:

$$\begin{aligned} H_2 &\rightarrow 2H^+ + 2e^- \\ Mo^{6+} + e- &\rightarrow Mo^{5+}(\text{blue color}) \end{aligned} \quad (3)$$

## Summary

In this paper, the blue colloidal $MoO_x$ were prepared by anodizing exfoliation method, which is a simple and fast approach. Colloidal nanoparticles have a plasmonic absorption peak at about 760 nm. Based on UV-vis spectrometry, TEM and chemical analysis, these colloidal nanosheets were able to reduce $HAuCl_4$ to gold nanoparticles of several nanometers in size, while they themselves were oxidized and loss their plasmonic peak. The resulting nanoparticles exhibited gasochromic coloration effect in the presence of hydrogen gas. In this process, the plasmonic absorption peak of Mo oxide raise again and its relative intensity was enhanced by increasing the amount of molybdenum oxide. Also, in this process, we observed a redshift in the gold plasmonic peak, which was attributed to an increase in the refractive index due to the change in the oxidation state of molybdenum oxide.

## References


1. Giljohann DA, Seferos DS, Daniel WL, Massich MD, Patel PC, Mirkin CA (2010) Gold nanoparticles for biology and medicine. Angew Chem Int Ed 49(19):3280–3294. https://doi.org/10.1002/anie.200904359
2. Huang X, Jain PK, El-Sayed IH, El-Sayed MA (2008) Plasmonic photothermal therapy (PPTT) using gold nanoparticles. Lasers Med Sci 23(3):217–228. https://doi.org/10.1007/s10103-007-0470-x
3. Jain PK, Huang X, El-Sayed IH, El-Sayed MA (2008) Noble metals on the nanoscale: optical and photothermal properties and some applications in imaging, sensing, biology, and medicine. Acc Chem Res 41(12):1578–1586. https://doi.org/10.1021/ar7002804
4. Lin CAJ, Yang TY, Lee CH, Huang SH, Sperling RA, Zanella M, Li JK, Shen JL, Wang HH, Yeh HI, Parak WJ, Chang WH (2009) Synthesis, characterization, and bioconjugation of fluorescent gold nanoclusters toward biological labeling applications. ACS Nano 3(2):395–401. https://doi.org/10.1021/nn800632j
5. Brust M, Walker M, Bethell D, Schiffrin DJ, Whyman R (1994) Synthesis of thiol-derivatised gold nanoparticles in a two-phase liquid–liquid system. J Chem Soc Chem Commun 7:801–802. https://doi.org/10.1039/C39940000801
6. Daniel MC, Astruc D (2004) Gold nanoparticles: assembly, supramolecular chemistry, quantum-size-related properties, and applications toward biology, catalysis, and nanotechnology. Chem Rev 104(1):293–346. https://doi.org/10.1021/cr030698+
7. Link S, El-Sayed MA (1999) Spectral properties and relaxation dynamics of surface plasmon electronic oscillations in gold and silver nanodots and nanorods. J Phys Chem B 103(40):8410–8426. https://doi.org/10.1021/jp9917648
8. Sun Y, Xia Y (2002) Shape-controlled synthesis of gold and silver nanoparticles. Science 298(5601):2176–2179. https://doi.org/10.1126/science.1077229
9. Turkevich J, Stevenson PC, Hillier J (1951) A study of the nucleation and growth processes in the synthesis of colloidal gold. Discuss Faraday Soc 11:55–75. https://doi.org/10.1039/df9511100055
10. Cai H, Yao P (2014) Gold nanoparticles with different amino acid surfaces: serum albumin adsorption, intracellular uptake and cytotoxicity. Colloids Surf B: Biointerfaces 123:900–906. https://doi.org/10.1016/j.colsurfb.2014.10.042
11. Scarabelli L, Sánchez-Iglesias A, Pérez-Juste J, Liz-Marzán LM (2015) A "tips and tricks" practical guide to the synthesis of gold nanorods. J Phys Chem Lett (6):4270−4279. ACS Publications
12. Murdoch M, Waterhouse G, Nadeem M, Metson J, Keane M, Howe R, Llorca J, Idriss H (2011) The effect of gold loading and particle size on photocatalytic hydrogen production from ethanol over Au/TiO2 nanoparticles. Nat Chem 3(6):489–492. https://doi.org/10.1038/nchem.1048
13. Subramanian V, Wolf EE, Kamat PV (2004) Catalysis with TiO2/gold nanocomposites. Effect of metal particle size on the fermi level equilibration. J Am Chem Soc 126(15):4943–4950. https://doi.org/10.1021/ja0315199
14. Astruc D, Lu F, Aranzaes JR (2005) Nanoparticles as recyclable catalysts: the frontier between homogeneous and heterogeneous catalysis. Angew Chem Int Ed 44(48):7852–7872. https://doi.org/10.1002/anie.200500766
15. Murphy CJ, Sau TK, Gole AM, Orendorff CJ, Gao J, Gou L, Hunyadi SE, Li T (2005) Anisotropic metal nanoparticles: synthesis, assembly, and optical applications. J Phys Chem B 109(29):13857–13870. https://doi.org/10.1021/jp0516846
16. Bastús NG, Comenge J, Puntes V (2011) Kinetically controlled seeded growth synthesis of citrate-stabilized gold nanoparticles of up to 200 nm: size focusing versus Ostwald ripening. Langmuir 27(17):11098–11105. https://doi.org/10.1021/la201938u
17. Henglein A, Meisel D (1998) Radiolytic control of the size of colloidal gold nanoparticles. Langmuir 14(26):7392–7396. https://doi.org/10.1021/la981278w
18. Langille MR, Personick ML, Zhang J, Mirkin CA (2012) Defining rules for the shape evolution of gold nanoparticles. J Am Chem Soc 134(35):14542–14554. https://doi.org/10.1021/ja305245g

19. Orendorff CJ, Murphy CJ (2006) Quantitation of metal content in the silver-assisted growth of gold nanorods. J Phys Chem B 110(9): 3990–3994. https://doi.org/10.1021/jp0570972
20. Sánchez-Iglesias A, Pastoriza-Santos I, Pérez-Juste J, Rodríguez-González B, García De Abajo FJ, Liz-Marzán LM (2006) Synthesis and optical properties of gold nanodecahedra with size control. Adv Mater 18(19):2529–2534. https://doi.org/10.1002/adma.200600475
21. Senthil Kumar P, Pastoriza-Santos I, Rodríguez-González B, De Abajo FJG, Liz-Marzán LM (2008) High-yield synthesis and optical response of gold nanostars. Nanotechnology 19(1):015606. https://doi.org/10.1088/0957-4484/19/01/015606
22. Geim AK, Novoselov KS (2007) The rise of graphene. Nat Mater 6(3):183–191. https://doi.org/10.1038/nmat1849
23. Novoselov KS, Jiang D, Schedin F, Booth TJ, Khotkevich VV, Morozov SV, Geim AK (2005) Two-dimensional atomic crystals. Proc Natl Acad Sci U S A 102(30):10451–10453. https://doi.org/10.1073/pnas.0502848102
24. Liu Y, Wang Z, Huang B, Yang K, Zhang X, Qin X, Dai Y (2010) Preparation, electronic structure, and photocatalytic properties of Bi2O2CO3 nanosheet. Appl Surf Sci 257(1):172–175. https://doi.org/10.1016/j.apsusc.2010.06.058
25. Ma Y, Jia Y, Wang L, Yang M, Bi Y, Qi Y (2016) Exfoliated thin Bi 2 MoO 6 nanosheets supported on WO 3 electrode for enhanced photoelectrochemical water splitting. Appl Surf Sci 390:399–405. https://doi.org/10.1016/j.apsusc.2016.08.116
26. Chhowalla M, Shin HS, Eda G, Li L-J, Loh KP, Zhang H (2013) The chemistry of two-dimensional layered transition metal dichalcogenide nanosheets. Nat Chem 5(4):263–275. https://doi.org/10.1038/nchem.1589
27. Wang F, Ueda W, Xu J (2012) Detection and measurement of surface electron transfer on reduced molybdenum oxides (MoOx) and catalytic activities of Au/MoOx. Angew Chem Int Ed 51(16):3883–3887. https://doi.org/10.1002/anie.201105922
28. Bai H, Yi W, Li J, Xi G, Li Y, Yang H, Liu J (2016) Direct growth of defect-rich MoO3−xultrathin nanobelts for efficiently catalyzed conversion of isopropyl alcohol to propylene under visible light. J Mater Chem A 4(5):1566–1571. https://doi.org/10.1039/C5TA08603E
29. Ressler T, Wienold J, Jentoft RE, Girgsdies F (2003) Evolution of defects in the bulk structure of $MoO_3$ during catalytic oxidation of propene. Eur J Inorg Chem (2):301–312
30. Dieterle M, Weinberg G, Mestl G (2002) Raman spectroscopy of molybdenum oxides. Phys Chem Chem Phys 4(5):812–821. https://doi.org/10.1039/b107012f
31. Amendola V, Meneghetti M (2009) Size evaluation of gold nanoparticles by UV−vis spectroscopy. J Phys Chem C 113(11):4277–4285. https://doi.org/10.1021/jp8082425
32. Adhikari S, Sarkar D (2014) Hydrothermal synthesis and electrochromism of WO3nanocuboids. RSC Adv 4(39):20145–20153. https://doi.org/10.1039/C4RA00023D
33. Delalat F, Ranjbar M, Salamati H (2016) Blue colloidal nanoparticles of molybdenum oxide by simple anodizing method: decolorization by PdCl 2 and observation of in-liquid gasochromic coloration. Sol Energy Mater Sol Cells 144:165–172. https://doi.org/10.1016/j.solmat.2015.08.038
34. Ranjba M, Delalat F, Salamati H (2017) Molybdenum oxide nanosheets prepared by an anodizing-exfoliation process and observation of photochromic properties. Appl Surf Sci 396:1752–1759. https://doi.org/10.1016/j.apsusc.2016.11.225
35. Yao J, Yang Y, Loo B (1998) Enhancement of photochromism and electrochromism in MoO3/Au and MoO3/Pt thin films. J Phys Chem B 102(11):1856–1860. https://doi.org/10.1021/jp972217u
36. Cheng H, Qian X, Kuwahara Y, Mori K, Yamashita H (2015) A plasmonic molybdenum oxide hybrid with reversible tunability for visible-light-enhanced catalytic reactions. Adv Mater 27(31):4616–4621. https://doi.org/10.1002/adma.201501172
37. Li N, Li Y, Sun G, Zhou Y, Ji S, Yao H, Cao X, Bao S, Jin P (2017) Enhanced photochromic modulation efficiency: a novel plasmonic molybdenum oxide hybrid. Nano 9(24):8298–8304
38. Angiola M, Alsaif MM, Kalantar-zadeh K, Wisitsoraat A, Wlodarski W, Martucci A (2015) Optical hydrogen sensing based on hybrid 2D MoO 3 /Au nanoparticles. Proc Eng 120:1141–1144. https://doi.org/10.1016/j.proeng.2015.08.830
39. Chen H, Xu N, Deng S, Lu D, Li Z, Zhou J, Chen J (2007) Gasochromic effect and relative mechanism of WO3 nanowire films. Nanotechnology 18(20):6. https://doi.org/10.1088/0957-4484/18/20/205701
40. Georg A, Graf W, Neumann R, Wittwer V (2000) Mechanism of the gasochromic coloration of porous WO3 films. Solid State Ionics 127(3-4):319–328. https://doi.org/10.1016/S0167-2738(99)00273-8
41. Lee SH, Cheong HM, Liu P, Smith D, Tracy CE, Mascarenhas A, Roland Pitts J, Deb SK (2001) Raman spectroscopic studies of gasochromic a-WO3 thin films. Electrochim Acta 46(13-14): 1995–1999. https://doi.org/10.1016/S0013-4686(01)00379-6
42. Wittwer V, Datz M, Ell J, Georg A, Graf W, Walze G (2004) Gasochromic windows. Sol Energy Mater Sol Cells 84(1-4):305–314. https://doi.org/10.1016/j.solmat.2004.01.040
43. Deng X, Quek SY, Biener MM, Biener J, Kang DH, Schalek R, Kaxiras E, Friend CM (2008) Selective thermal reduction of single-layer MoO3 nanostructures on Au(111). Surf Sci 602(6):1166–1174. https://doi.org/10.1016/j.susc.2008.01.014
44. He T, Ma Y, Cao Y, Yin Y, Yang W, Yao J (2001) Enhanced visible-light coloration and its mechanism of MoO3 thin films by Au nanoparticles. Appl Surf Sci 180(3-4):336–340. https://doi.org/10.1016/S0169-4332(01)00370-1
45. Karuppasamy L, Chen CY, Anandan S, Wu JJ (2017) High index surfaces of Au-nanocrystals supported on one-dimensional MoO 3 -nanorod as a bi-functional electrocatalyst for ethanol oxidation and oxygen reduction. Electrochim Acta 246:75–88. https://doi.org/10.1016/j.electacta.2017.06.040
46. Pan H, Zuo L, Fu W, Fan C, Andreasen B, Jiang X, Norrman K, Krebs FC, Chen H (2013) Organic Electronics: physics, materials, applications. 14:797–803
47. Tu AG, Zhou X (2010) OLEDs with Au/$MoO_3$ hole injection layer. Faguang Xuebao/Chin J Luminescence 31(2):157–161
48. Tan X, Wang L, Cheng C, Yan X, Shen B, Zhang J (2016) Plasmonic MoO3−x@MoO3nanosheets for highly sensitive SERS detection through nanoshell-isolated electromagnetic enhancement. Chem Commun 52(14):2893–2896. https://doi.org/10.1039/C5CC10020H
49. Yan W, Petkov V, Mahurin SM, Overbury SH, Dai S (2005) Powder XRD analysis and catalysis characterization of ultra-small gold nanoparticles deposited on titania-modified SBA-15. Catal Commun 6(6): 404–408. https://doi.org/10.1016/j.catcom.2005.04.004
50. Chithambararaj A, Bose AC (2011) Investigation on structural, thermal, optical and sensing properties of meta-stable hexagonal MoO3nanocrystals of one dimensional structure. Beilstein J Nanotechnol 2:585–592. https://doi.org/10.3762/bjnano.2.62
51. Huang Q, Hu S, Zhuang J, Wang X (2012) MoO3-x-based hybrids with tunable localized surface plasmon resonances: chemical oxidation driving transformation from ultrathin nanosheets to nanotubes. Chem Eur J 18(48):15283–15287. https://doi.org/10.1002/chem.201202630
52. Rouhani M, Foo YL, Hobley J, Pan J, Subramanian GS, Yu X, Rusydi A, Gorelik S (2013) Photochromism of amorphous molybdenum oxide films with different initial Mo5+ relative concentrations. Appl Surf Sci 273:150–158. https://doi.org/10.1016/j.apsusc.2013.01.218
53. Ahmad MZ, Golovko VB, Adnan RH, Abu Bakar F, Ruzicka J-Y, Anderson DP, Andersson GG, Wlodarski W (2013) Hydrogen

sensing using gold nanoclusters supported on tungsten trioxide thin films. Int J Hydrog Energy 38(29):12865–12877. https://doi.org/10.1016/j.ijhydene.2013.07.089

54. Shakir I, Shahid M, Kang DJ (2010) MoO3 and Cu0.33MoO3 nanorods for unprecedented UV/Visible light photocatalysis. Chem Commun 46(24):4324–4326. https://doi.org/10.1039/c000003e
55. Lim B, Camargo PH, Xia Y (2008) Mechanistic study of the synthesis of Au nanotadpoles, nanokites, and microplates by reducing aqueous HAuCl4with poly(vinyl pyrrolidone). Langmuir 24(18):10437–10442. https://doi.org/10.1021/la801803z
56. Anbananthan N, Nagaraja Rao K, Venkatesan VK (1994) Cyclic voltammetric investigations of the reduction of Mo(VI) to Mo(IV) in 1 M sulphuric acid. J Electroanal Chem 374(1-2):207–214. https://doi.org/10.1016/0022-0728(94)03356-0
57. Mendoza-Sánchez B, Brousse T, Ramirez-Castro C, Nicolosi V, Grant PS (2013) An investigation of nanostructured thin film α-MoO3 based supercapacitor electrodes in an aqueous electrolyte. Electrochim Acta 91:253–260. https://doi.org/10.1016/j.electacta.2012.11.127
58. Patil RS, Uplane MD, Patil PS (2006) Structural and optical properties of electrodeposited molybdenum oxide thin films. Appl Surf Sci 252(23):8050–8056. https://doi.org/10.1016/j.apsusc.2005.10.016
59. Castillero P, Rico-Gavira V, López-Santos C, Barranco A, Pérez-Dieste V, Escudero C, Espinós JP, González-Elipe AR (2017) Formation of subsurface W5+species in gasochromic Pt/WO3 thin films exposed to hydrogen. J Phys Chem C 121(29):15719–15727. https://doi.org/10.1021/acs.jpcc.7b03385
60. Luther JM, Jain PK, Ewers T, Alivisatos AP (2011) Localized surface plasmon resonances arising from free carriers in doped quantum dots. Nat Mater 10(5):361–366
61. Naik GV, Kim J, Boltasseva A (2011) Oxides and nitrides as alternative plasmonic materials in the optical range [Invited]. Optical Mater Express 1(6):1090–1099. https://doi.org/10.1364/OME.1.001090
62. Manthiram K, Alivisatos AP (2012) Tunable localized surface plasmon resonances in tungsten oxide nanocrystals. J Am Chem Soc 134(9):3995–3998. https://doi.org/10.1021/ja211363w
63. Chen Y-H, Franzreb M, Lin R-H, Chen L-L, Chang C-Y, Yu Y-H, Chiang P-C (2009) Platinum-doped TiO2/magnetic poly(methyl methacrylate) microspheres as a novel photocatalyst. Ind Eng Chem Res 48(16):7616–7623. https://doi.org/10.1021/ie900509t
64. Jiang J, Liu J, Peng S, Qian D, Luo D, Wang Q, Tian Z, Liu Y (2013) Facile synthesis of α-MoO3 nanobelts and their pseudocapacitive behavior in an aqueous Li2SO4 solution. J Mater Chem A 1(7):2588–2594. https://doi.org/10.1039/c2ta01120d